Continuum limit of amorphous elastic bodies:
A finite-size study of low-frequency harmonic vibrations

A. Tanguy,* J. P. Wittmer, F. Leonforte, and J.-L. Barrat

Département de Physique des Matériaux, Université Claude Bernard & CNRS, 69622 Villeurbanne Cedex, France

The approach of the elastic continuum limit in small amorphous bodies formed by weakly polydisperse Lennard-Jones beads is investigated in a systematic finite-size study. We show that classical continuum elasticity breaks down when the wavelength of the solicitation is smaller than a characteristic length of approximately 30 molecular sizes. Due to this surprisingly large effect ensembles containing up to $N = 40\,000$ particles have been required in two dimensions to yield a convincing match with the classical continuum predictions for the eigenfrequency spectrum of disk-shaped aggregates and periodic bulk systems. The existence of an effective length scale ξ is confirmed by the analysis of the (non-Gaussian) noisy part of the low frequency vibrational eigenmodes. Moreover, we relate it to the *nonaffine* part of the displacement fields under imposed elongation and shear. Similar correlations (vortices) are indeed observed on distances up to $\xi \approx 30$ particle sizes.

I. INTRODUCTION

Determining the vibration frequencies and the associated displacement fields of solid bodies with various shapes is a well studied area of continuum mechanics[1–3] with applications in fields as different as planetary science and nuclear physics. The increasing development of materials containing nanometric size structures leads one to question the limits of applicability of classical continuum elasticity theory, which is in principle valid only on length scales much larger than the interatomic distances.[3,4] This question is relevant from an experimental viewpoint, since mechanical properties are inferred from spectroscopic measurements systematically interpreted within the framework of continuum elasticity.[5–8] As increasingly smaller length scales are now investigated,[8] direct verification of this assumption is highly warranted.

For macroscopic systems, on the other side, it is well known that the vibrational density of states in amorphous glassy materials deviates from the classical spectrum at the so called "Boson peak" frequency which is in the Terahertz range.[9–12] The nature of the "Boson peak" is highly controversial.[14,15] However, this experimental fact suggests that continuum theory is inappropriate at small length scales where the disorder of the amorphous system may become relevant.[13] Obviously, one may ask if there is a finite length scale below which the classical mechanical approach becomes inappropriate, and what the microscopic features are which determine it.[4,14–16] Elaborating further the brief presentation given in Ref. 13, we show by means of a simple generic simulation model that, indeed, a relatively large characteristic length exists, and, second, that it envolves collective particle rearrangements.

The above questions are more generally related to the propagation of waves in disordered materials,[17] and concern foam[25] and emulsions[24] as well as granular materials,[18–20,26] when they are submitted to small amplitude vibrations. As for these systems of current interest, the existence of an elastic limit is still a matter of debate,[22] we believe that the detailed characterization of strongly heterogeneous elastic benchmark systems with a well defined continuum limit approach is crucial.

In this paper, we investigate the existence of a continuum limit in the vibrational modes of two-dimensional amorphous nanometric Lennard-Jones materials. The objects we consider are either disk-shaped clusters of diameter $2R$, as the one shown on the left-hand side of Fig. 1, or bulk-like systems without surfaces contained in a square of side L with periodic boundary conditions [Fig. 1(b)]. Technically, the systems are formed by carefully quenching a slightly polydisperse liquid of spherical particles interacting via simple Lennard-Jones (LJ) pair potentials into the nearest energy minimum. Due to the polydispersity the resulting structures are isotropic and *amorphous*, i.e., exhibit no long range crystalline order. The force network (Fig. 1) appears to be strongly varying with weak and tensile zones (red) embedded within a rigid repulsive skeleton (black). These "force chains" are very similar to those found in cohesionless granular media without attractive forces.[21] This feature may be added to the list of similarities which have been noticed between granular and amorphous (glassy) materials.[22–24] As the force network is strongly inhomogeneous, the relevance of the quenched stresses is a natural question.[4]

We investigate the vibrational modes of these objects using atomic level simulations. All particle coordinates and interparticle forces are exactly known here, and it is possible to calculate the vibration frequencies around an equilibrium position, by exact diagonalization of the so-called dynamical matrix[27] expressible in terms of the first and second derivatives of the interparticle interaction potentials. We have carried out a systematic comparison of these eigenfrequencies $\omega(p)$ (p being an index increasing with frequency) obtained numerically with those predicted by continuum elasticity for two-dimensional objects of increasingly large sizes.[1] We concentrate on the lowest end of the vibrational spectrum, since this is the part that corresponds to the largest wavelengths for the vibrations, and should reach first the continuum limit. These frequencies are also those which are
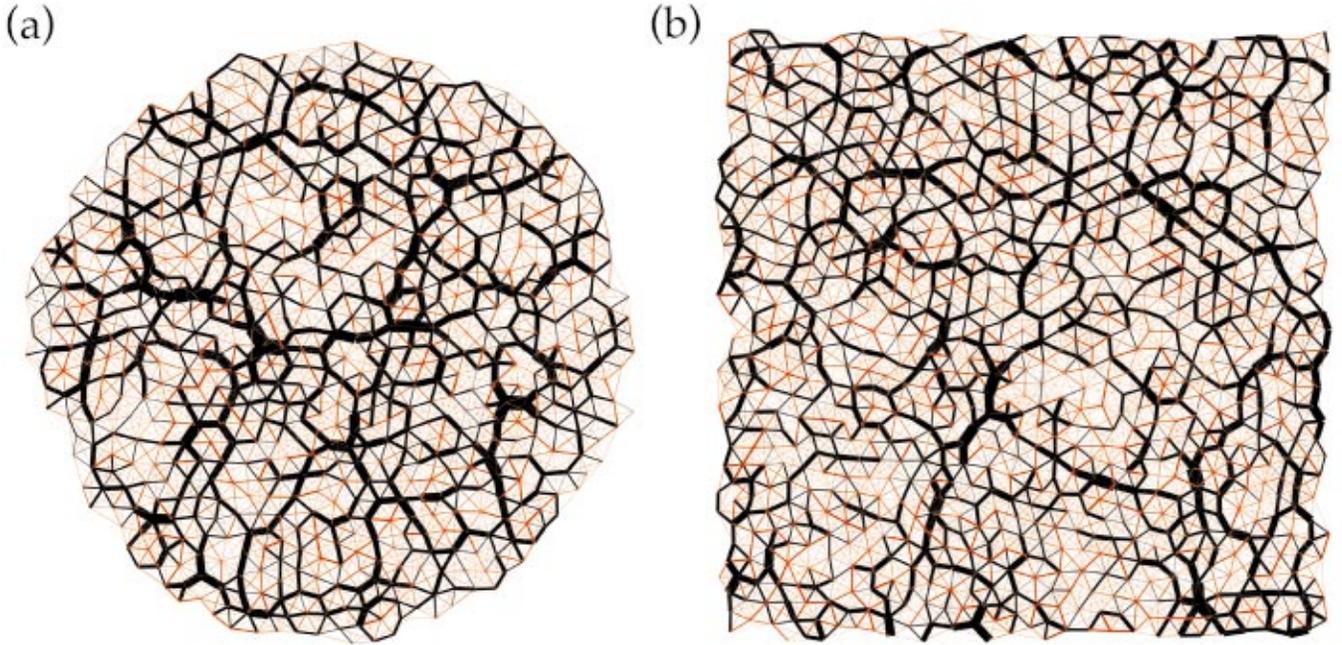
FIG. 1. (Color) Representation of the network of quenched stresses in two small quenched Lennard-Jones particle systems in two dimensions: (a) a disk-shaped aggregate of diameter $2R \approx 32a$ containing $N = 732$ particles (protocol I) on the left and (b) a periodic bulk system with $L = 32.9a$ and $N = 1000$ (protocol III) on the right-hand side. The line scale is proportional to the tension transmitted along the links between beads. The black lines indicate repulsive forces (negative tensions), while the red links represent tensile forces between the verticies. Both shown networks are very similar despite different symmetries and quench protocols. They are strongly inhomogeneous and resemble the pattern seen in granular materials. Zones of weak attractive links appear to be embedded within the strong skeleton of repulsive forces.

probed in low frequency Raman scattering experiments,[8] in order to determine the typical size of nanoparticles.

The key result of this paper is to show the existence of a characteristic wavelength (thus a characteristic size) beyond which the classical continuum limit is valid, but below which it is erroneous. Moreover, we show the existence of rotational structures (vortices) of similar sizes, when the system is submitted to simple mechanical sollicitations (traction and shear). The size of these vortices is relatively large (≈ 30 average interatomic distances). We discuss the relation between the sizes of the vortices and the limit of applicability of the classical continuum theory by computing the elastic moduli, by studying the symmetry of the nanoscale stress tensor, and by identifying the low frequency vibrational eigenmodes.

Our paper is arranged as follows: In Sec. II we summarize some basic relations and results of classical continuum theory for two-dimensional elastic bodies. Simulation techniques, sample parameters, and preparation protocols of our model amorphous systems are explained in Sec. III and simple system properties are discussed. In Sec. IV we analyze histograms and spatial correlations of the quenched forces and of the stiffness of the bonds. A weak enhancement of the rigid skeleton is demonstrated for small systems. The next two sections contain the key results of this paper. In Sec. V we discuss the mechanical properties of a periodic bulk system under elongation and shear, we compute the elastic moduli and we characterize the nonaffine displacement field generated. The eigenvalues and eigenvectors and

their departures from the continuum prediction are analyzed in Sec. VI. We conclude with a summary of our results in Sec. VII.

II. THEORY

A. Continuum description of an isotropic elastic body in 2D

The so-called *classical* continuum theory of elasticity[28] is a theory that proposes to describe an elastic solid at a macroscopic level. Its main assumption (by opposition to *nonclassical* continuum theories like Cosserat elasticity or others) is that the system can be entirely described by a unique vector field: the displacement field $\underline{u}(\underline{r})$, describing the displacement of a volume element from its equilibrium position $\underline{r}$. In systems at zero temperature, energy and free energy are identical. The Landau expansion[2] of the energy δE per unit volume is expressed in terms of $\underline{u}$ and its first derivatives. Due to translational and rotational invariance[28] of δE, it depends only up to second order on the symmetric part of $\mathbf{grad}\,\underline{u}$, the (linearized) strain tensor $\epsilon_{\alpha\beta} \equiv 1/2\,(\partial u_\alpha / \partial x_\beta + \partial u_\beta / \partial x_\alpha)$ with $x_1 = x$ and $x_2 = y$ for the coordinates. Moreover in linear elasticity (that is in the lowest order in the Landau expansion), for isotropic and homogeneous systems only two Landau parameters are required, thus in the absence of any external field,

$$\delta E = \frac{\lambda}{2}(\epsilon_{xx} + \epsilon_{yy})^2 + \mu(\epsilon_{xx}^2 + \epsilon_{yy}^2 + 2\epsilon_{xy}^2), \quad (1)$$

where we have defined the two phenomenological Lamé coefficients λ and μ. μ is the so-called shear modulus, and λ is related to the compressibility $K = \lambda + \mu$. The stress tensor can be defined as the conjugate variable of the strain tensor,

$$\sigma_{\alpha\beta} \equiv \partial \delta E / \partial \epsilon_{\alpha\beta}. \tag{2}$$

In this definition $\sigma_{\alpha\beta}$ is obviously a symmetric tensor. We will see later that a *microscopically* constructed stress tensor can, however, violate this symmetry condition at small length scales (Sec. V). Using Eq. (2), we obtain the Hooke's relations that are used in Sec. V to measure directly the Lamé coefficients from the forces generated in a macroscopic periodic box under external strain.

As it is well known,[1,2] the equations of motion $\rho \partial \sigma_{\alpha\beta} / \partial x_{\alpha} = \ddot{u}_{\alpha}$ together with the constitute Hooke's relations correspond to wave equations with boundary conditions depending on the problem of interest: for the periodic box problem the solutions must have the same periodicity, and the freely floating disk-shaped aggregate requires vanishing lateral and radial stresses on its surface. The velocities of transverse and longitudinal waves which solve these wave equations are given in terms of the Lamé coefficients, i.e., one has $c_T^2 = \mu/\rho$, and $c_L^2 = (\lambda + 2\mu)/\rho$ where ρ is the particle density.[1] We are reminded that $c_L > c_T$ and that transverse modes thus correspond generally to smaller eigenfrequencies.

The solutions for the periodic box case are of course the plane waves with a wave vector quantified by the boundary conditions, $(k_x, k_y) = (2\pi/L)(n, m)$, with wavelength[29]

$$\lambda(p) = \lambda(n,m) = \frac{2\pi}{||\underline{k}||} = \frac{L}{(n^2 + m^2)^{1/2}} \tag{3}$$

and with dimensionless frequency

$$\Omega_{T,L}^2(p) \equiv \left(\frac{\omega(p)L}{2\pi c_{T,L}} \right)^2 = n^2 + m^2, \tag{4}$$

with two quantum numbers $n, m = 0, 1, \ldots$. The running index p increases with frequency. In the continuous case, the dispersion relation is linear, and the frequency is straightforward. Hence, eigenfrequencies are characterized by a pair of different integers. They are eightfold degenerated if $n \neq m \neq 0$ and fourfold in all other cases. The associated plane waves travel in two opposite and orthogonal directions.

The situation for disk-shaped objects is somewhat more complex,[1] with again two quantum numbers n and k characterizing the eigenmodes. The quantum number k is associated with the angular dependency of the displacement field (and is due to the 2π periodicity), and the number n to its radial dependency. The eigenfrequencies are obtained by solving the nonlinear dispersion relation. They are of the form,

$$\Omega_{T,L}^2(p) \equiv \left(\frac{\omega(p)2R}{2\pi c_{T,L}} \right)^2 = f_{nk}(\nu), \tag{5}$$

where $\nu = \lambda/(\lambda + 2\mu)$ is the Poisson ratio.[30] The eigenvectors are related to Bessel functions[1] which may be approx-

mated locally by plane waves if $\lambda(p) \ll R$. Vibrational modes of disks are either non degenerate (for axially symmetric modes) or have twofold degeneracy (for all other modes). Indeed, for $k > 0$, for every solution whose amplitude is $\propto e^{ik\theta}$, one finds a second solution, orthogonal to the first one, with amplitude $\propto e^{ik(\theta + \Delta\theta)}$, where $\Delta\theta = \pi/2k$. Every additional solution with the same k is a linear combination of these two vectors. For axially symmetric modes ($k = 0$), the above argument does not apply; any additional solution found by turning the coordinate system is identical to the first one.

We finally stress the obvious: degenerate eigenvalues are inherent to the continuum treatment of highly symmetric systems. The failure to observe them indicates either the lifting of the relevant symmetry or the breakdown of continuum theory.

B. Pair potential systems with central forces

In a simulation one has the advantage to know all the individual contributions to the total energy. The situation is particularly simple if one has to deal with interparticle pair potentials $U(r_{ij})$ (r_{ij} being the interparticle distance) such as the LJ potential we use, and if we stay at zero temperature. In this case, the difference of the total potential energy,

$$E_p = \sum_{i=1}^{N-1} \sum_{j>i}^{N} U(r_{ij}) \tag{6}$$

due to a displacement field $\underline{u}$ can be written to second order as a Hessian form $\delta E_p = \frac{1}{2} \underline{u}^t \cdot \underline{\underline{M}} \cdot \underline{u}$ in terms of the $(2N) \times (2N)$ *dynamical matrix* $\underline{\underline{M}}$ whose elements are given for $i \neq j$ by

$$-r_{ij}^2 M_{i\alpha, j\beta} = r_{ij} t_{ij} (\delta_{\alpha\beta} - n_\alpha n_\beta) + r_{ij}^2 c_{ij} n_\alpha n_\beta, \tag{7}$$

$$M_{i\alpha, i\beta} = -\Sigma_j M_{i\alpha, j\beta}, \tag{8}$$

n being the unit vector of the bond (for simplicity, we do not indicate the dependence of n on the particle indices i and j), $t_{ij} \equiv \partial U(r_{ij})/\partial r_{ij}$ the tension and $c_{ij} \equiv \partial^2 U(r_{ij})/\partial r_{ij}^2$ the stiffness of the bond between two interacting beads i and j. The first one is related to the stresses "quenched" in the bulk, but as we will see later it is in general small in comparison with the second one. As in the present study the mass m of each monomer is set equal to unity (even though the particle diameters are polydisperse) the Euler–Lagrange equation $\underline{\underline{M}} \cdot \underline{u} + m\ddot{\underline{u}} = 0$ is solved directly by diagonalization of the dynamical matrix which yields the eigenfrequencies as eigenvalues and the corresponding displacement fields as eigenvectors.

A central aspect of this work concerns the possible role of the nonaffine displacement field which is neglected at macroscopic level. In order to compare this assumption with our results, it is useful to estimate the elastic moduli with an hypothetical affine displacement field. Assuming *constant* deformations under elongation and shear, one may use the dynamical matrix expression of the free energy to calculate

TABLE I. Some properties characterizing disk-shaped clusters generated by a slow aggregation following protocol I with MD steps at $T = 0.1, 0.05, 0.01, 0.005$, and 0.001. We have indicated the particle size N, the number of configurations in the ensemble M, the radius R_i of the initial sphere, the mean radius R of the final globule, the mean density ρ, the excentricity e obtained from the inertia tensor of the cluster, the interaction energy per particle E, the Lamé coefficients λ_a, and μ_a obtained using Eq. (9) and the mean spring constant $\langle r_{ij}^2 c_{ij} \rangle$. The mean tension $\langle r_{ij} t_{ij} \rangle$ and, hence, the pressure are too tiny to be measured accurately.

N	M	R_i/a	R/a	ρ	e	E	λ_a	μ_a	$\langle r_{ij}^2 c_{ij} \rangle$
8192	5	54	53.5	0.912	0.25	-2.81	24.8	24.9	31.9
10 000	6	60	59.1	0.912	0.21	-2.81	24.8	24.9	31.9
16 384	4	85	76.9	0.882	0.16	-2.80	23.9	24.1	32.0
32 768	1	120	109.9	0.864	0.11	-2.80	23.5	23.1	32.0

the Lamé coefficients. Comparing[31] the Landau expression Eq. (1) and the microscopic energy information in Eq. (6) yields

$$\lambda_a = \frac{1}{A} \sum_{ij} [r_{ij} t_{ij} n_x^2 n_y^2 + r_{ij}^2 c_{ij}((n_x^4 + n_y^4)/2 - 2n_x^2 n_y^2)],$$
$$\tag{9}$$
$$\mu_a = \frac{1}{A} \sum_{ij} r_{ij}^2 c_{ij} n_x^2 n_y^2,$$

with A being the total surface. The sums run over all pairs of particles. As an *affine* displacement field is assumed to be valid down to atomic distances the coefficients have been assigned an index a to distinguish them from the true macroscopic Lamé coefficients that will be calculated later. Note that this is a crude approximation[32] that is widely used but can give strong errors on the estimate elastic moduli, as already mentioned in Ref. 4. We will test the affinity assumption in Sec. V and estimate the length below which the affine approximation becomes problematic.

III. SAMPLE PREPARATION AND CHARACTERIZATION

Systems with two different boundary conditions (disks and periodic bulk systems) and three quench protocols have been simulated. In this section we discuss some technical points concerning the simulation methods and the sample preparation protocols and parameters. The details of the protocols and some properties of the final configurations are summarized in the Tables I, II, and III.

In the present study we use a shifted LJ potential[34] for polydisperse particles. Natural LJ units are used, i.e., we set the energy parameter $\epsilon \equiv 1$, the particle mass $m \equiv 1$, and the mean diameter $a = \langle a_i \rangle = 1$. Note that while the particle mass is strictly monodisperse the particle diameters a_i are homogeneously distributed between 0.8 and 1.2, corresponding to a polydispersity index $\delta a/a \approx 0.12$ which is sufficient to prevent large scale crystalline order. We did not attempt to make the particles even more polydisperse fearing demixing or systematic radial variation of particle sizes in the case of disk-shaped aggregates.

TABLE II. Some properties characterizing disk-shaped clusters generated with the fast quench protocol II which takes advantage of already quenched periodic bulk systems (protocol III). As in the first table we indicate the radius R_i of the initial disk, the number of configurations in the ensemble M, the (mean) particle number, the mean density ρ, the excentricity e, the interaction energy per particle E, the Lamé coefficients λ_a, and μ_a and the mean spring constant $\langle r_{ij}^2 c_{ij} \rangle$. The final cluster radius is not given as it is essentially identical to R_i. Note that in the second protocol the particle number N fluctuates (very weakly) around its mean value $\langle N \rangle$ while it is a constant operational parameter in the first protocol. The excentricity is much smaller here than in the first more realistic protocol. The information contained in the last four columns is very similar to the one in the corresponding columns of Table I and Table III despite the fact that different quench protocols have been used.

R_i/a	M	$\langle N \rangle$	ρ	e	E	λ_a	μ_a	$\langle r_{ij}^2 c_{ij} \rangle$
52	5	7848	0.917	0.08	-2.81	24.9	24.9	31.9
60	8	10 448	0.919	0.05	-2.81	25.0	25.1	31.9
85	8	20 968	0.917	0.06	-2.82	25.1	25.0	31.8
120	4	37 030	0.910	0.04	-2.84	25.9	25.9	32.9

The quench generally starts with molecular dynamics (MD) at some fixed temperature using a simple velocity rescaling thermostat.[34,35] The temperature remains constant over a fixed time interval of 1000 unit time for each temperature step (see the caption of the tables for more details). This was sufficient to relax systems into a steady-state (obviously, not necessarily the equilibrium) as monitored by pressure and system energy. Unfortunately, no more detailed characterization of the aging as a function of the quench rate has been recorded. Following the initial MD sequence we quench the systems further down using an overdamped (OD) algorithm. Finally, the conjugate gradient method (CG) (Refs. 35 and 36) was iterated until the configurations reach their local energy minima.

An example for a disk-shaped aggregate has already been presented in Fig. 1(a). Two different protocols have been employed to generate such disks:

Protocol I: The starting point of the first protocol is a not too dense LJ liquid droplet of radius R_i and $\rho_i \approx 0.9$ and temperature $T_i = 0.1$. The initial radius R_i is chosen such that the final mean radius R becomes not too different. We cool the systems with MD steps at decreasingly small T. As described above, we finally quench each system into its local minimum using a sequence of OD and CG steps. See Table I for details.

Protocol II: In the second case spherical disks of radius R_i were cut out of amorphous periodic systems already prepared at $T = 0$ (see Protocol III) and $\rho = 0.925$ and the disks are quenched as before with OD and CG. No finite temperature MD step was included here. See Table II for details. The second protocol is much faster than the first one which might, however, mimic better the actually occurring aggregation process in real systems.

The radius $R = \sqrt{2(I_1 + I_2)/N}$ of quenched cluster is obtained from the eigenvalues $I_1 > I_2$ of the inertia tensor of the cluster. The mean density $\rho = \langle N/\pi R^2 \rangle$ obtained accordingly

TABLE III. Some properties characterizing periodic bulk systems generated following protocol III with MD steps at $T=1.0$, 0.5, 0.1, 0.05, 0.01, 0.005, and 0.001. In addition to properties also recorded in the previous tables we have included here the Lamé factors λ and μ obtained from a macroscopic deformation and the mean tension $\langle r_{ij}t_{ij} \rangle$. Note that $\langle r_{ij}^2 c_{ij} \rangle \gg \langle r_{ij}t_{ij} \rangle$.

N	L/a	ρ	M	E	P	λ	μ	λ_a	μ_a	$\langle r_{ij}t_{ij} \rangle$	$\langle r_{ij}^2 c_{ij} \rangle$
5000	73.5	0.925	20	-2.84	0.29	39.6	11.3	26.2	26.5	-0.09	33.1
10 000	110	0.826	1	-2.78	-0.63	14.5	7.5	18.4	18.4	0.22	28.2
10 000	109	0.841	1	-2.81	-0.61	20.4	8.3	20.0	19.5	0.21	28.3
10 000	108	0.857	1	-2.81	-0.67	21.2	7.8	20.1	19.7	0.23	28.0
10 000	107	0.873	1	-2.81	-1.06	23.1	8.0	18.9	17.9	0.36	25.8
10 000	106	0.890	1	-2.82	-1.13	25.3	8.9	18.0	17.4	0.38	25.4
10 000	105	0.907	1	-2.84	-0.48	31.0	11.0	22.4	22.5	0.16	29.2
10 000	104	0.925	20	-2.84	0.25	39.5	11.7	26.2	26.4	-0.19	32.9
10 000	103	0.943	1	-2.83	1.24	47.4	13.3	31.3	31.4	-0.38	37.8
10 000	102	0.961	1	-2.78	2.71	59.5	14.9	37.7	39.3	-0.77	44.0
10 000	101	0.980	1	-2.72	4.25	69.7	18.8	44.7	46.6	-1.15	50.1
10 000	100	1.000	1	-2.62	5.96	84.0	19.0	51.9	54.8	-1.55	56.4
20 000	147.1	0.925	3	-2.84	0.35	40.4	12.0	26.8	27.0	-0.11	33.4
40 000	208	0.925	2	-2.84	0.33	-	-	26.7	27.1	-0.11	33.3

is a weakly decreasing function of the particle number. This is expected and in qualitative agreement with the decreasing Laplace pressure $P \propto 1/R$. Note that the pressure is very small for all the disks (Protocol I and II alike) and is not indicated. We have also tried to characterize the shape of the disks and have indicated the eccentricity $e = \sqrt{1 - I_2/I_1}$. As can be seen, small aggregates are strongly elliptic, but the effect is much stronger for the first slow aggregation protocol. This is probably due to capillary waves formed at $T = 0.1$ which are subsequently frozen in. Obviously, ellipticity is one possible cause for lifting of the eigenfrequency degeneracy. This effect should, however, become small for larger clusters where e vanishes (Tables I and II). Moreover, we will see later that the mechanical properties of our aggregates do not depend significantly on the quench protocol.

Periodic bulk systems, such as the one presented in Fig. 1(b), have been prepared following a third protocol described here. We started with equilibrated liquids at $T = 1$ which were then cooled down in successive temperature steps (as detailed in the caption of Table III). Systems between $L = 7a$ and $L = 208a$ and containing from $N = 50$ up to $N = 40\,000$ particles have been sampled.

For $N = 10\,000$ particles we have systematically scanned over density varying the box size from $L = 100$ to $L = 110$. This was done in order to find—for the given protocol—a working point density for which large bulk systems correspond to a near zero pressure state $P(T=0) \approx 0$, thus the mechanical properties of the bulk systems correspond to the free-floating aggregates. Note that only one configuration has been sampled for this measurement sequence. As a sideline, we draw attention to the fact that systems with $P < 0$ while mechanically stable in a periodic box are thermodynamically unstable at low temperature. If more time would be given to the systems to equilibrate as allowed by the protocol phase separation would occur. Indeed we find evidence for the formation of small holes for $\rho < 0.85$. In all other cases we find

that density is perfectly homogeneous down to a scale typical of the interatomic distance and density fluctuations are easily excluded as a microscopic candidate for explaining the slow continuum approach. Our systematic finite-size study, i.e., the variation of box sizes L, was performed at fixed density $\rho = 0.925$. In order to scale correctly the eigenfrequencies of the aggregates we have also recorded the Lamé coefficients as a function of density. We have checked that the particle energies E, Lamé factors λ_a and μ_a, mean effective spring constants $\langle r_{ij}^2 c_{ij} \rangle$ (which are included in the different tables) do not depend significantly on the different symmetries and quench protocols, for a given density. It is reassuring that all the results we obtained are robust with regard to the variation of the quench protocol even though history dependence must obviously play a role for the details. Typically, we have generated 20 configurations for each L and in terms of CPU hours this was the most demanding part of this study. The simulations have been performed on a local workstation cluster over a period of 1 year.

Interestingly, we notice in Table III that the pressure, the particle energy, and the Lamé coefficient λ increase systematically in small boxes. This is shown specifically for λ in Fig. 4(b). These finite-size effects indicate correlations on a similar length even in larger systems. We will now turn to the characterization of these correlations, by first studying the dynamical matrix, and the quenched stresses.

IV. CONTRIBUTIONS TO THE DYNAMICAL MATRIX: QUENCHED FORCES AND SPRING CONSTANTS

In this section we discuss various distributions and correlation functions associated with the quenched particle positions, forces and spring constants which contribute to the dynamical matrix [Eq. (7)]. We attempt a characterization of the frozen in disorder visualized in Fig. 1, where the snapshots reveal strong spatially correlated fluctuations. Specifi-
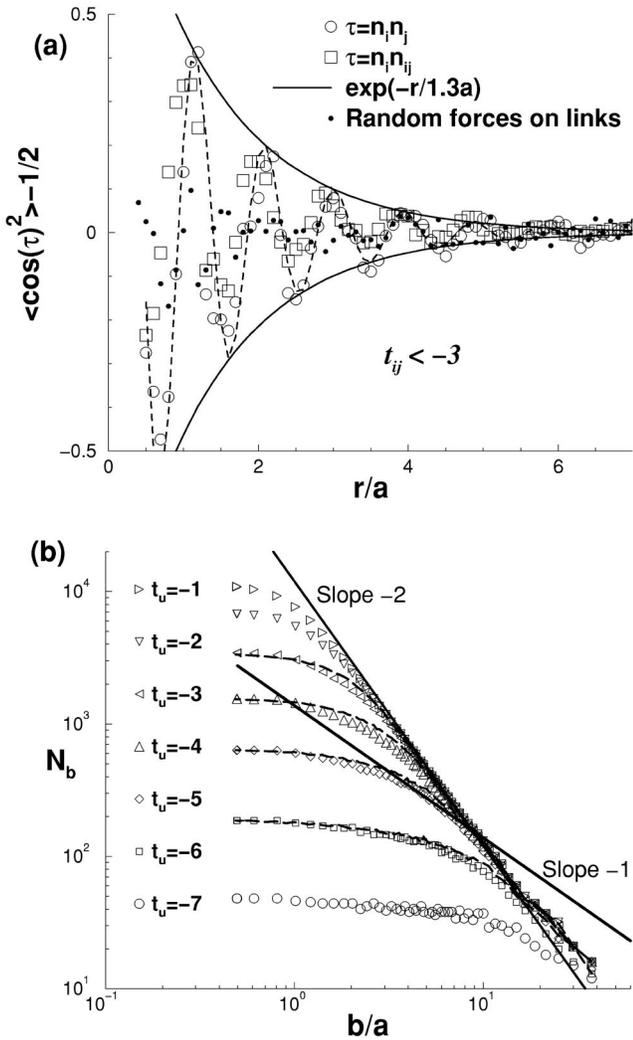
FIG. 2. Correlations of frozen in forces for large periodic systems: (a) pair correlation $\langle \cos^2(\tau) \rangle$ versus distance r. Here τ denotes either the angle between the directors n_i and n_j of the links i and j (symbols) or the angle between the director n_i of link i and the direction n_{ij} between the links i and j (lines). The decay of the envelope is exponential with a length scale of the order of the mean bead size, hence, this does not introduce a new length scale. The dots correspond to an artificial force network obtained by shuffling randomly the tensions between existing links. The sinusoidal dashed line is a guide for the eyes. (b) The number N_b of boxes of size b needed to cover the interactions transmitting repulsive tensions smaller than t_u. The curves do not differ much from box counting results on sets of randomly drawn links (dashed lines). Different slopes are included for comparison. The slope -1 corresponds to linear chain-like structures, the -2 slope to a compact structure in 2D.

cally, we ask if it is possible to extract a characteristic length scale solely from the distribution of weak and rigid regions which might be a candidate to explain the large crossover length scale ξ mentioned in the Introduction. We start by giving some additional information concerning the snapshots, turn then to the histograms and discuss finally the fractal structure of the quenched forces.

A timely justification for discussing quenched forces lies in the current interest of their role in granular materials, foams, and glassy colloidal systems.[4,21–26] It has been suggested by Alexander[4] and others that the quenched forces might contribute to the unusual mechanical and rheological properties in these systems. However, to put this immediately into perspective, quenched forces are unlikely candidates to rationalize alone the slow continuum approach discussed in Sec. VI, basically, since their *average* contribution to the dynamical matrix is weak: $\langle r_{ij}^2 c_{ij} \rangle \gg \langle r_{ij} t_{ij} \rangle$. This inequality is revealed in Table III. Note that, due to this result, the possible contribution of a linear term in the macroscopic expression (1) for δE is not relevant to explain our results. We come back to this in Sec. VI where we discuss the contribution of the quenched forces to the eigenmodes.

The second and more important point we want to make here is that both first (quenched stresses) and second (stiffnesses of the bonds) derivatives of the given potential are expressions of the same disorder generated by the complex cooling procedure; it is the final positional disorder which matters, not the individual contributions to the dynamical matrix. If the width of the lines between the particle positions shown in the snapshots (Fig. 1) has been chosen proportional to the interaction force rather than the spring constant this was done mainly for *artistic* reasons. Resembling snapshots can be obtained, using as a scale for the line width either the spring constants or the trace $m_{ij} = M_{ix,jx} + M_{iy,jy}$ of the dynamical submatrices. Such pictures are direct visualizations of the dynamical matrix.

The snapshots in Fig. 1 reveal that the structure of the force network is very inhomogeneous, but isotropic on larger scale. They show also evidently that the quenched disorder is not much affected by the different symmetries (circle or square) and quench protocols. This corroborates the robustness of the system properties with regard to the chosen protocol mentioned in the previous section. This is also supported by the different histograms regrouped in Fig. 3.

Systems of the three protocols are included in first of both graphs Fig. 3(a) where we discuss the distribution of distances of interacting particles (inset) r_{ij}/r_0 and of the tensile forces t_{ij} (main figure) for relatively large systems containing $N = 10\,000$ particles. Comparison shows that there is essentially no dependence on quench protocol. Note that this is only a technical point and will make life easier when we analyze the eigenvalue spectrum of disk-shaped aggregates. The peak at $r_{ij} = r_0$ in the inset corresponds to the peak for $t_{ij} = 0$ in the main figure of Fig. 3(a). Hence, most of the interactions have achieved to minimize their energy although this is not required for global mechanical stability. The distribution of the repulsive forces (negative tensions) is Gaussian. Incidentally, this is quite different from the recently reported exponential force distributions in granular matter.[21,23] Interestingly however, the tail of the force distribution becomes more and more exponential upon decreasing of the system size. We do not show this here, as the same effect is presented in the second panel [Fig. 3(b)] for the trace of the dynamical submatrices. Various system sizes as indicated in the figure are given here for the third protocol at $\rho = 0.925$. This demonstrates that the tail of distribution, which corresponds to very rigid contacts, becomes enhanced due to
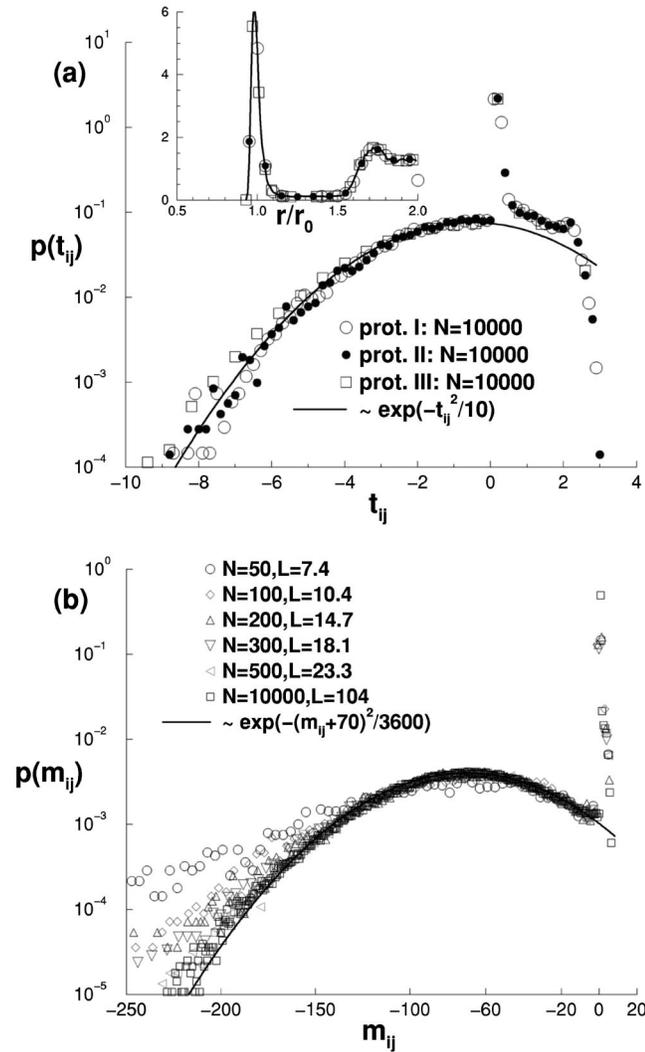
FIG. 3. Histograms of contributions to the dynamical matrix: (a) comparison of the tension t_{ij} for all three protocols at $N=10\,000$. Inset: Histogram of distances r_{ij}/r_0 of interacting particles. (b) Trace of matrix $m_{ij}=M_{xi,xj}+M_{yi,yj}$ for systems of various system sizes as indicated in the figure (protocol I). This demonstrates finite-size effects in the tail of the distributions of small systems with $L<20$ corresponding to an enhancement of the skeleton of very rigid contacts.

finite-size effect for systems below $L\approx20a$. A very similar figure could be shown for the distribution of spring constants. Note that the peak on the left-hand side of Fig. 3(b) is due to the slow variation of the spring constant for large distances and corresponds to distances seen in the shoulder on the right of the histogram in the inset.

In Fig. 2 we show two of several attempts to analyze the correlations and fractal structure of force chains (or the spring constants) in view of extracting a characteristic size. We focus on strong repulsive forces and strong positive spring constants. Only results from the first measurements are reported as both yield similar results. In a first step we obtain the network of all interactions with (negative) repulsive tensions above some threshold t_u and compute then on these sets various correlation functions. The functions

$\langle\cos^2(\tau)\rangle$ traced in Fig. 2(a) attempt to put the visual impression of linear force chains in quantitative terms. Here τ denotes either the angle between the directors n_i and n_j of the links i and j (spheres) or the angle between the director n_i of link i and the direction n_{ij} between the links i and j (squares). The difference between the two methods is small. The correlation dies out only after about six oscillations. No significant difference have been found by increasing or decreasing the threshold t_u. The decay of the envelope is exponential with a length scale of the order of the mean bead size. Hence, while rigid regions seems to be spatially correlated, this does not, apparently, introduce a new length scale. Note that the situation is similar in granular materials.[20]

The second part of Fig. 2 shows a direct attempt to elucidate the fractal structure of the network of quenched forces by means of the standard box counting technique. Here we count the number of square boxes of linear size b needed to cover all the links between beads carrying a repulsive force smaller than t_u. For small b where every box contains only one link the differential fractal dimension is zero. In the opposite limit where the boxes are much larger than the average distance between links, the differential fractal dimension must equal the spatial dimension, i.e., $d_f=2$. The power law slope $d_f=1$ in between both limits indicates the typical distance where the contact network with $t_{ij}<t_u$ has a linear chain-like structure. For example, we find a tangent with slope $d_f=1$ at $b\approx6a$ for $t_u=-5$. This distance is strongly increasing if we focus on more and more rigid subnetworks (decreasing t_u). Note, however, that there is no *finite* b-window with $d_f=1$ and in a strict sense there is again no characteristic length scale associated with linear structures. A simple visual inspection of Fig. 1 that would suggest a characteristic length scale of the repulsive force network much larger than the interatomic separation is apparently incorrect and possibly caused by the natural tendency of our brains to emphasize linear patterns.[37]

As a simple benchmark for the spatial correlation of the force network, we have distributed links randomly. The box counting of these uncorrelated links gives the dashed lines. Unfortunately, these are virtually identical to the fractal dimension characterization of the force chains in the LJ systems and it is a very tiny difference (at least in this characterization) which is related to the spatial correlations. Obviously, this does not mean the forces are uniformly distributed as clearly shown by the snapshots and by the large number of oscillations in the correlation function.

In summary, we provide evidence for a strong dispersion in the dynamical matrix, i.e., in the *local* elastic properties of our systems. Although linear chain like structures exist apparently, this does *not* give rise to an additional characteristic length—defined as the screening length in an exponential decay—much larger than the mean particle distance.

V. ELONGATION AND SHEAR: ELASTIC MODULI AND NONAFFINE DISPLACEMENT FIELD

A direct way of illustrating the failure of classical elasticity at small scales is to investigate the displacement field in a large, deformed sample. If the system is uniformly strained

at large scales, e.g., by compressing or shearing a rectangular simulation box, classical elasticity implies that the strain is uniform at all scales, so that the atomic displacement field should be affine with respect to the macroscopic box deformation. If this is true Eqs. (9) should provide reliable estimates of the Lamé coefficients. Since the latter can be independently measured in a computer experiment from the generated stress differencies using Hooke's Law [Eqs. (2)] this provides a direct and crucial test for the affinity assumption.

Our numerical test proceeds in three steps:

(1) Each initial configuration is given a first quick CG quench with *quadruple* precision to have a more precise estimate for the unstrained reference system. This is necessary since the stress differences we compute are very small for strains in the linear response regime and the numerical accuracy of double precision simulation runs turns out to be insufficient.

(2) Second, we perform an affine strain of order ϵ of both the box shape and the particle coordinates. We consider both an elongation in x-direction $[L_x \rightarrow L_x(1+\epsilon), r_x \rightarrow r_x(1+\epsilon)]$ and a pure shear using Lees-Edwards boundary conditions[34] together with $r_x \rightarrow r_x + r_y \epsilon$. [We refer here to the principal box particle coordinates (r_x, r_y) of the periodic configurations.]

(3) Finally, we quench with CG the configurations into the local minima while maintaining the strain at the boundaries. For given boundary conditions in the linear regime the solution must be unique.

The differences of particle positions, forces and total energies computed at each step are recorded. We stress that this procedure is technically not trivial and that great care is needed to measure physically sound properties.

We have systematically varied ϵ over several orders of magnitude from $\epsilon = 10^{-3}$ down to $\epsilon = 10^{-9}$ (not shown). The induced displacement field is reversible and linear in the amplitude of the imposed initial strain for an initial strain in a window $10^{-7} \leq \epsilon \leq 10^{-4}$ which decreases (for unknown reasons) somewhat with system size. Obviously, for higher strains the linearity of Eq. (2) must eventually break down. The departure from linearity below the given strain window is due to numerical accuracy.

Using Eq. (2) for the stress tensor averaged on the whole system and the averaged strain field, we obtain the true macroscopic Lamé coefficients λ and μ. Within the given strain window the measured λ and μ coefficients are strain independent, thus confirming the linearity of the elastic response in this range. The values of μ and λ are presented in Fig. 4 where we have compared them with the affine field predictions. (Note that the Poisson ratio $\nu \approx 2/3$ is larger than $1/2$ which is permissible in a 2D.[30]) The coefficients relying on a negligible nonaffine field [open symbols, obtained from Eq. (9)] differ by a factor as large as 2 from the true ones. Clearly, a calculation taking into account the nonaffine character of the displacements is necessary for disordered systems. It is simple to work out from the values given in the figures that, in a simple elongation, a finite energy fraction $(\lambda_a + 2\mu_a)/(\lambda + 2\mu) - 1 \approx 1/4$ of the total strain can be recovered from the nonaffine displacements. In a pure shear,
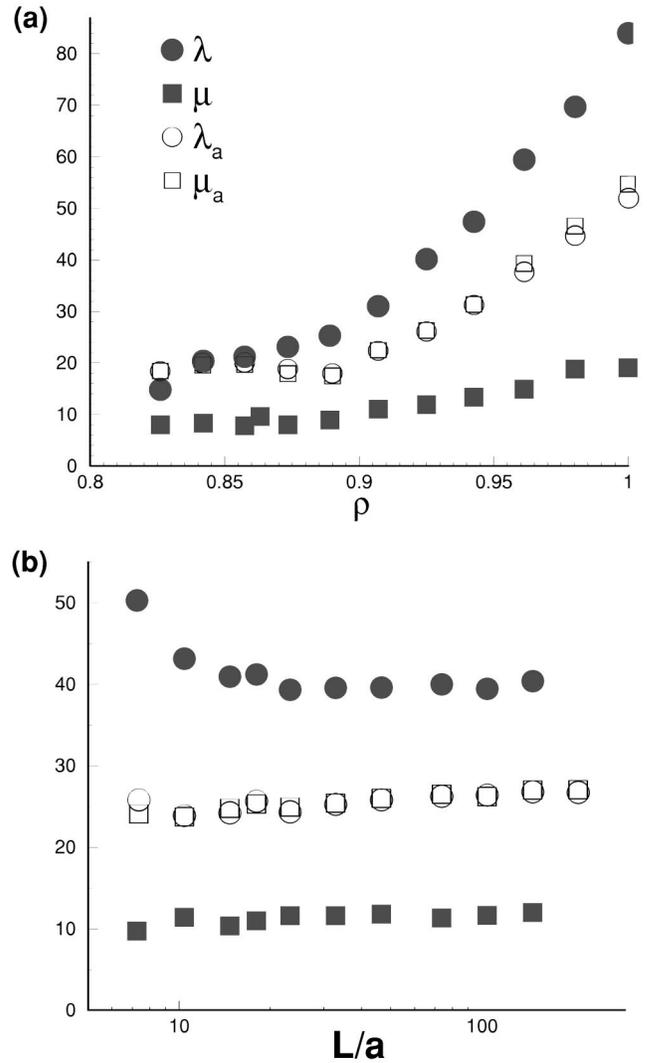
FIG. 4. Lamé coefficients λ and μ obtained for periodic bulk systems: (a) density variation for $N = 10\,000$, (b) size variation for $\rho = 0.925$. Full symbols correspond to the direct measurement using Hooke's law, open symbols are obtained using Eqs. (9). Naturally, all Lamé coefficients rise with density as the number and strength of pair interactions increases. Note that while μ remains more or less constant λ increases with decreasing L in a similar way as pressure and particle energy (Table III).

the energy fraction $\mu_a / \mu \approx 1/2$ is even larger; only the compressibility $K = \lambda + \mu$ remains unchanged. Hence, in quantitative terms the nonaffinity of the atomic displacements is not a negligible effect.

The nonaffine component δu of the atomic displacement field in large systems subject to an elongation in x direction is illustrated in the snapshot of Fig. 5(a). A similar snapshot holds in case of a pure shear [Fig. 5(b)]. In some regions, the displacement is much larger than expected from a purely affine transformation. (Note that even the nonaffine part of the displacement field is strictly linear in ϵ within the strain interval indicated above.) Local displacements transverse to the direction of the elongation are allowed, and organize coherently into vortices. The transversal direction thus cannot
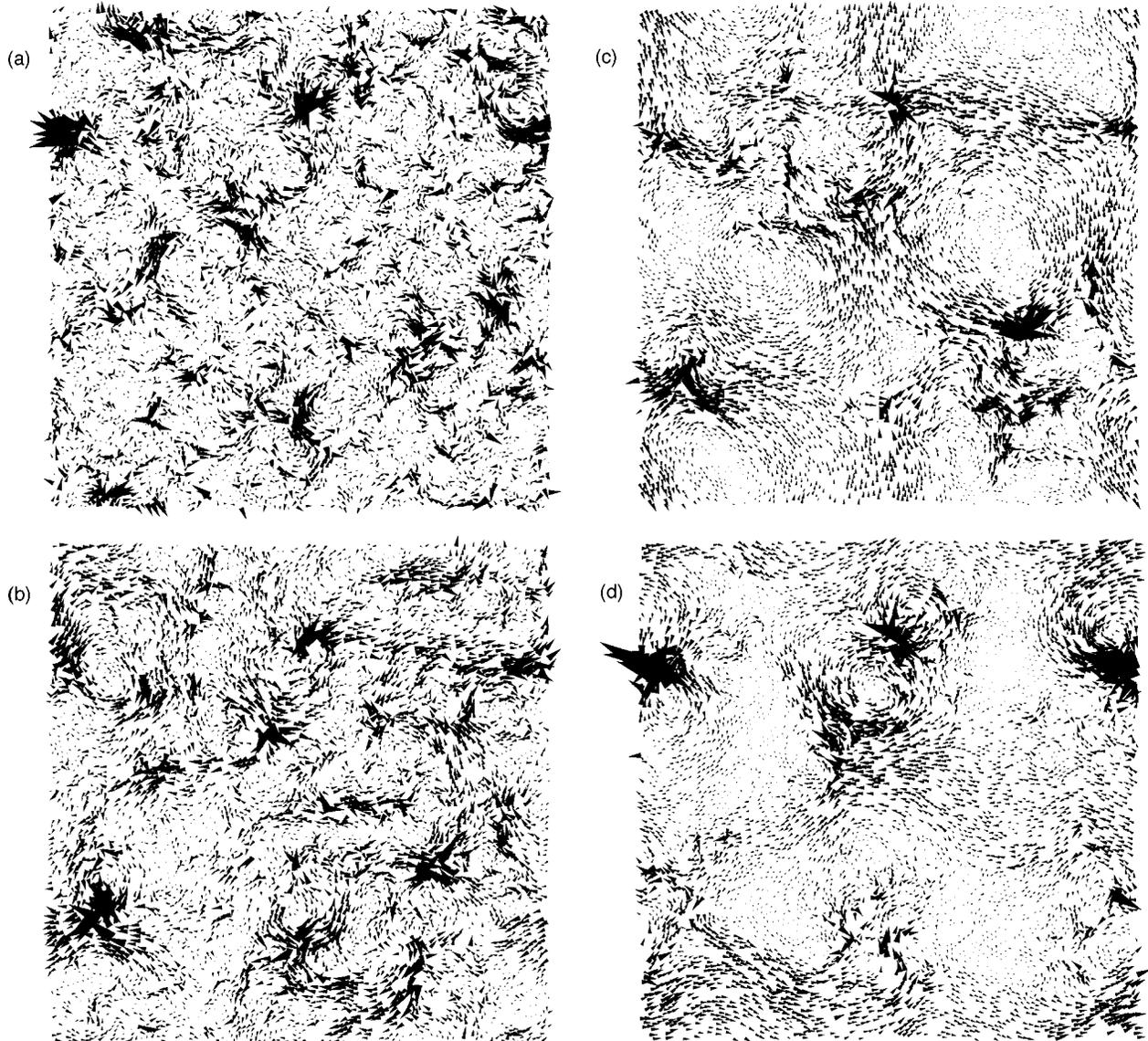
FIG. 5. Comparison of nonaffine displacement field $\delta u(r)$ with eigenvector field $\delta v_p(r)$ for periodic box of size $L=104a$ containing $N=10\,000$ particles: (a) nonaffine displacement field under elongation in x direction, (b) same for plain shear using Lees–Edwards boundary conditions (Ref. 34), (c) eigenvector field for $p=3$, and (d) eigenvector field for $p=7$. This confirms that the different noise fields are *non-Gaussian* and are highly correlated in space and with respect to each other. Detailed inspection shows vortices like in turbulent flow.

be neglected, showing that the modelling approach put forward in Ref. 18 is not realistic. The crossover length ξ mentioned in the Introduction manifests itself through *correlated deviations* from a purely affine displacement. Visual inspection tells us that the sizes of the vortices and $\xi \approx 30a$ are comparable.

The two correlation functions presented in Fig. 6 confirm this visual impression. The first one shows the correlation function $C_u(r) = \langle \delta u(r) \cdot \delta u(0) \rangle$. The striking anticorrelation for $r \lesssim 30a$ is in agreement with the size of the vortices seen in the displacement fields. That the displacement field is indeed correlated over a similar size is further elucidated in Fig. 6(b). Here we consider the systematic coarse-graining of the nonaffine displacement field

$$\delta \mathcal{U}_j \equiv \frac{1}{N_j} \sum_{i \in V_j} \delta u(r_i) \tag{10}$$

of all N_j beads contained within the square volume element V_j of linear size b. The mean-squared average $U_x(b) \equiv \langle \delta \mathcal{U}_{x,j}^2 \rangle_j^{1/2}$ is plotted versus the size of the coarse-graining volume element b. We have normalized the function by its value at $b=1$. The coarse-grained field decreases very weakly for $b<30a$ and only for much larger volume elements we find the power law slope -1 expected for uncorrelated events. As for symmetry reasons the total or mean nonaffine field vanishes we have $U_x(b \to L) \to 0$ for very large volume elements. Apart from this trivial system size

FIG. 7. Asymmetry of the stress tensor of the forces generated in simple shear (Lees–Edwards boundary conditions) for a system containing 10 000 particles. We measure the ''microscopic stress'' acting on a volume element as shown in the sketch on the right. In the main figure we plot the average mean-squared stress difference $\langle(\sigma_{xy}-\sigma_{yx})^2\rangle^{1/2}$ versus the linear size b of the volume element. For small box sizes $b<30a$ we evidence power law behavior which crosses to an exponential decay at large volume sizes.

FIG. 6. Characterization of nonaffine displacement field δu-field obtained by simple elongation: (a) correlations function $C_u(r)=\langle\delta u(r)\cdot\delta u(0)\rangle$, (b) mean coarse-grained field $U_x(b)/U_x(\overline{b}=1)$ versus the size b of the coarse-graining. Both functions become system size independent for large L. The first figure on the left-hand side shows clearly an anticorrelation in agreement with the vortices seen in the snapshot in Fig. 5(a).

dependence U_x approaches a system size independent envelope for $b\ll L$, as can be clearly seen from the figure.

Barely distinguishable functions have been obtained for U_y (not depicted) which demonstrates the isotropy of the nonaffine displacement fields which may also be inferred straight from the snapshots and appropriately chosen correlations functions. Similar characterizations can be obtained from a standard Fourier transform of $\delta u(x,y)$ and from the gradient fields defined on the coarse-grained field $\delta \mathcal{U}_j$. These are again not presented.

In the rest of this section, we consider the local stresses generated by the applied macroscopic deformation. We show in Fig. 7 the variance $\langle(\sigma_{xy}-\sigma_{yx})^2\rangle$ averaged on various boxes of size b. Here, the stress tensor $\sigma_{\alpha\beta}$ has been defined, as in classical mechanics, as the average force per unit length exerted in the α direction through the side perpendicular to the β direction of the volume element of size b. Note that

this definition of the stress tensor, does *not* correspond strictly to the usual[4,33] microscopic Kirkwood definition $(-\Sigma_j t_{ij} n_\alpha . n_\beta)$ which is necessarily symmetric. Both quantities yield the same macroscopic stress tensor, but the definition *we* are using is more appropriate to illustrate deviations from macroscopic behavior at small scales. We see clearly in the Fig. 7 that for a size $b<30a$, this stress tensor is asymmetric, and that the asymmetry decreases exponentially to zero for larger sizes. The usual, macroscopic proof[2,3] of the symmetry of $\sigma_{\alpha\beta}$ is based on the fact that intermolecular forces are short-ranged. Hence, one expects symmetry of the microscopic stress tensor (obtained from the '''macroscopic'' definition) only for volume elements of size b much larger than the range of intermolecular forces. However, as very recently pointed out in Ref. 33, the *microscopic* stress tensor needs not to be symmetric. The well known *macroscopic* argument does not apply due to the local disorder and the resultant contribution to the elastic energy of the work of the fluctuating forces on the fluctuating part of $\overline{u}$. It was shown in Ref. 33 that this last contribution vanishes only for very large systems.

We note that the length scales observed in all these plots are relatively large compared to the particle size, but are *not* in the classical sense characteristic lengths appearing in the exponential decay of a correlation function. An important consequence of the large spatial correlations is that calculations of Lamé coefficients are prone to finite-size effects for system sizes similar and below ξ. This explains qualitatively the peculiar system size dependence of the Lamé coefficients reported in Fig. 4(b).

VI. VIBRATION MODES

In this section we discuss finally the eigenvalues and eigenvectors of the different systems we have generated. For

each configuration the lowest ($p \leq 1000$) vibration eigenfrequencies and eigenvectors have been determined using the version of the Lanczos method implemented in the PARPACK numerical package.[38] As stressed in the Introduction we concentrate on the lowest end of the vibrational spectrum, since this is the part that corresponds to the largest wavelengths for the vibrations.

We continue and finish first the discussion of disk-shaped aggregates which started with the snapshot Fig. 1(a). This being done we focus more extensively on the simpler periodic glassy systems (Protocol III) and discuss subsequently their eigenfrequencies and eigenvectors. This allows us to pay attention to central questions of strongly disordered elastic materials without being sidetracked by additional physics at cluster boundaries (ellipticity, radial variation of material properties, etc.).

A. Eigenmodes of disk-shaped aggregates

The first nontrivial eigenvalues ($4 \leq p \leq 11$) for the two protocols for disk-shaped clusters are shown in Fig. 8(a). The first three eigenmodes have vanishing eigenfrequencies because of two translational and one rotational invariance. Aggregates of different sizes are presented as indicated in the figure. The frequencies are rescaled with the disk diameter $2R$ as suggested by dimensional considerations or continuum theory. This scaling is roughly successful for all systems included. For the smaller systems (e.g., for the example with $N = 732$ given) ω do not present the degeneracies of the continuum theory. If we increase the system size steps appear and the eigenfrequencies start to regroup in pairs of two following the continuum prediction. This is well verified for the largest disk we have created containing $N = 32\,768$ beads. The horizontal lines are comparisons with continuum theory with appropriate density and where the Lamé coefficients (and, hence, the sound velocities) have been taken accordingly from Table III. The comparison of the two protocols (I and II) for $N = 4096$ shows that, perhaps surprisingly, the quench protocol does not matter much if only the clusters are large enough and the excentricity sufficiently weak. Note that this is definitely not true for small disks where the excentricity matters.

The next step is now to characterize the continuum approach as a function of system size. Our analysis presented in Fig. 9(a) is similar to the finite-size studies of phase transitions and critical phenomena. The rescaled eigenfrequencies for given p are plotted vs the rescaled inverse system size $\xi/2\langle R \rangle$ in such a way that the vertical axis $\Omega^2 = \langle (\omega R / \pi c)^2 \rangle$ should become independent of the cluster properties (size, density, Lamé coefficients) in the limit of large systems. ξ is the crossover length defined in the previous section. We have taken $\xi \equiv 30a$. The horizontal lines correspond to the continuum predictions for quantum numbers (n,k) as indicated. Both axes are dimensionless. For the p given in the figure only transversal modes are expected and, hence, we have used the transversal sound velocity $c = c_T(\rho)$ everywhere. For $p < 14$ all modes should be twofold degenerated and one expects even (full symbols) and odd (open symbols) modes to regroup in pairs. This is born out

(a)

○ N=723, 2R=32a
□ N=4096, 2R=75.4a
△ N=32768, 2R=220a
■ <N>=4180, 2R=76a

(b)

○ L=33a, N=1000
□ L=208a, N=40000
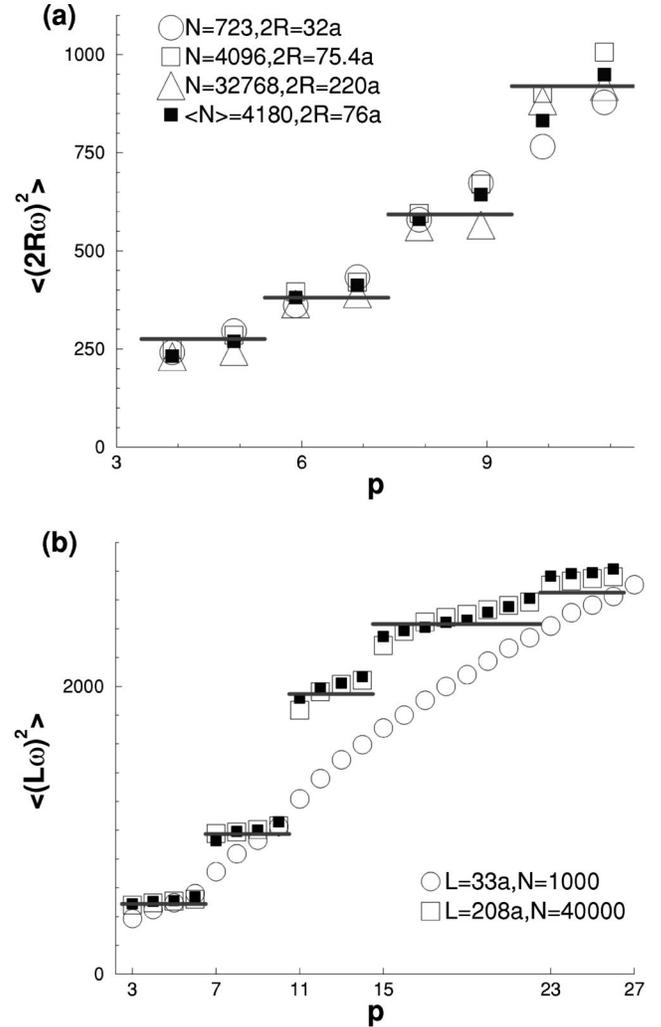
FIG. 8. Comparison of the first nontrivial eigenvalues for (a) disk-shaped clusters and (b) bulk systems confirming the predicted degeneracies for sufficiently large samples. In small systems, the degeneracy is lifted. The frequencies are rescaled with the system size (as indicated) and compared with the theoretical predictions (horizontal lines). The open symbols in (a) correspond to the slow quench (protocol I), the full symbols to a rapid quench (protocol II) showing that the results of both protocols become similar for large disks. The open and full squares in (b) correspond to two different configurations with the same parameters.

for the larger systems; for $2\langle R \rangle \gg \xi$ the lowest frequencies even match *quantitatively* the predictions. There is no adjustable parameter left for the vertical scale. The crossover at $\xi/2\langle R \rangle \approx 1$ for the smallest eigenfrequencies justifies the (somewhat arbitrary) choice of the numerical value of ξ. Interestingly, the continuum limit is approached in a *nonmonotonous* fashion and very small systems vibrate at higher frequencies. One cause for this is certainly the higher excentricity of smaller clusters. As we will see below, however, additional and more fundamental physics plays also a role.

Every data point corresponds to an average over an ensemble with identical operational parameters. The number of configurations in every ensemble have been chosen such that the (not indicated) error bar is of the order of the symbol
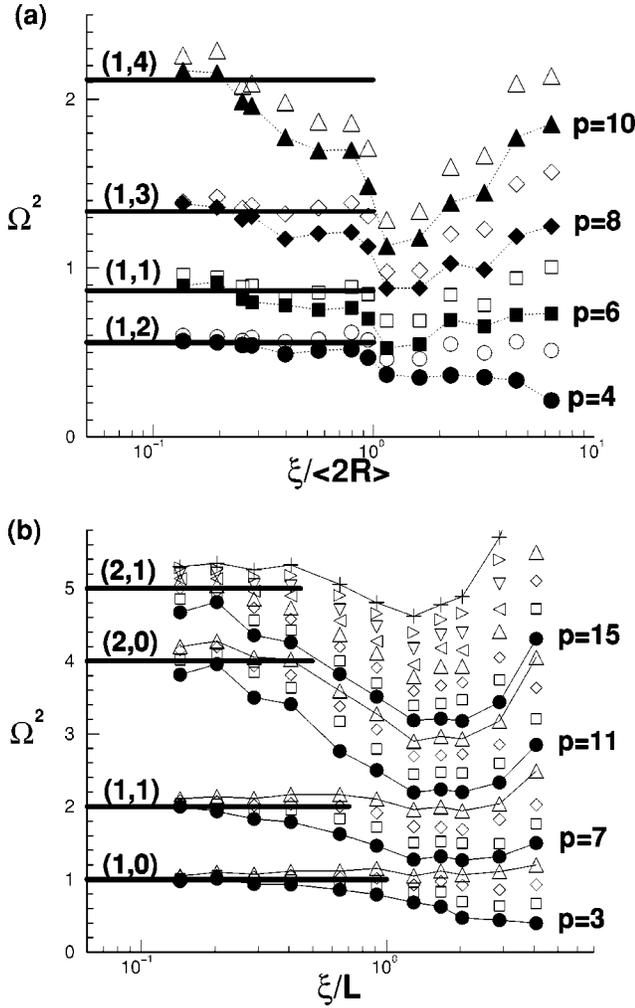
FIG. 9. Finite-size scaling of reduced eigenfrequencies $\Omega^2(p,L) = \langle (\omega(p,L)L/2\pi c_T)^2 \rangle$ versus ξ/L with $\xi \equiv 30a$: (a) disk-shaped aggregates from protocol I with $L=2R$, (b) periodic bulk systems at $\rho=0.925$ (protocol III). The mode index p increases from bottom to top, some of the p are specifically given (full symbols). In both cases the degeneracy is systematically lifted for small systems and the continuum prediction (given by the horizontal lines) is approached nonmonotoneously. The pairs of quantum numbers (n,k) and (n,m) associated with the predictions are indicated in (a) and (b), respectively.

size. The dispersion of an individual measurement is much larger, however, for smaller systems and of the order of the frequency difference between subsequent modes $\omega(p+1)^2 - \omega(p)^2$. As the problem seems to be strongly self-averaging, as one expects, the dispersion between different representations of an ensemble goes strongly down with system size. Note that the diameters $2R$ and the densities ρ of each configuration in an ensemble vary somewhat and we have used in the averaging procedure the sound velocities associated with every specific sample density. This was done by means of interpolating the numerical values of the Lamé coefficients shown in Fig. 4(a). The dispersion of sound velocities within an ensemble is, however, relatively weak even though the Lamé coefficients depend strongly on density.

We have presented in the figure data from the first protocol of elaboration. Data from the second protocol looks quite similar. For small systems there are differences probably due to the higher eccentricity as mentioned above. As some of the results presented here, such as the nonmonotonous variation, could be due to spurious surface and excentricity effects in circular systems, we now turn our attention for the rest of this section to the periodic glassy systems.

B. Eigenfrequencies of periodic bulk systems

Raw data for eigenfrequencies for systems generated following the third protocol are given in Fig. 8(b) for two examples at $\rho=0.925$. As there is no rotational invariance in a periodic box only the first two modes $p=1$ and $p=2$ vanish. The vibration frequencies do not display the degeneracies of the continuum in the smaller system with $L=32.9$ (spheres). It appears that the finite-size effects are much more pronounced in the eigenfrequencies compared to the weak effects discussed in Fig. 3(b) on the stiffness. In contrast to small systems, the degeneracy steps are clearly visible for the largest configurations (square symbols) we have sampled with $N=40\,000$. The quantitative agreement with continuum prediction is then satisfactory and deteriorates only slightly with increasing p, i.e., with decreasing wavelength $\lambda(p)$. Two configurations have been obtained in the latter case (open and full symbols). Interestingly, the self-averaging is such that both are barely different, even where they depart from the classical theory.

Figure 9(b) shows the eigenfrequencies for bulk systems as a function of box size L in analogy to the characterization presented above for disks. The horizontal axis is now ξ/L, the vertical axis $\Omega^2 = \langle (\omega L/2\pi c_T)^2 \rangle$. While the continuum approach is somewhat smoother in the bulk case than for the disks essentially both sets of data shown in Fig. 9 carry the same message: They indicate that for system sizes L below ξ the predictions of continuum elasticity become erroneous even for the smallest eigenmodes. The classical degeneracy of the vibration eigenfrequencies is lifted and the resulting density of states, becomes a continuous function. The approach of the elastic limit is again nonmonotonous. This is not related to the dispersion due to the discreteness of an atomic model, which would result into a monotonous approach to the elastic limit, as can be easily checked on one-dimensional models. As we have no surface effects here the effect must be due the frozen-in disorder. Obviously, the physics at play should also be relevant for the disk-shaped clusters.

As a sideline we report here briefly that we have also investigated the role of the quenched stresses on the eigenfrequency spectrum. This can be readily done by switching off the contribution from the tensions in the dynamical matrix Eq. (7). The corresponding *artificial* system appears to remain mechanically stable (i.e., all eigenvalues remain positive), however, it does not correspond to any realistic interaction potential. A finite-size plot analog to the ones shown in Fig. 9 has been computed for periodic systems. This yields a result *qualitatively* very similar to the curves presented here, albeit the crossover to continuum occurs for slightly

smaller box sizes. The point we want to make here is two-fold: On the one side quenched forces matter if it comes to *quantitative* comparisons and evaluation of an analytical model, on the other hand, they do not generate new physics. The role of quenched stresses is simply to maintain a local equilibrium in systems with strong positional disorder. The results presented here, and particularly the deviation from classical continuum theory, appears to be due to local disorder and simple harmonic but disordered couplings would give analogous results.

As in the study of critical phenomena where finite-size effects reveal correlations at wavelengths $\lambda(L,p)$ in much larger systems where $L \gg \lambda$ one naturally expects that the results of Fig. 9 are also relevant for the description of higher eigenmodes and their departure from continuum theory. We demonstrate in Fig. 10 that the crossover to continuum is indeed characterized by the ratio of wavelength and the correlation length ξ. The numerical eigenfrequencies Ω are rescaled by their expectation $\Omega_{\text{cont}}(n,m)$ from continuum theory [Eq. (4)] and plotted vs the inverse wavelength $\xi/\lambda_{\text{cont}}(n,m)$, where the wavelength is inferred from Eq. (3) for the quantum numbers n and m associated with the mode index p. Again we set (to some extend arbitrarily) $\xi \equiv 30a$. As can be seen, all the data sets obtained for various sizes collapse and confirm within numerical accuracy the choice of the scaling variables. Interestingly, *two* separate scaling functions appear for transverse and longitudinal modes and, for clarity, we have plotted both in two different graphs. The crossover occurs at about $\lambda_{\text{cont}} \approx \xi$ for the transverse modes in agreement with the observations in Fig. 9(b). In contrast, about twice as large wavelengths are required for longitudinal modes to obtain a satisfactory match with continuum theory as shown in Fig. 10(b). Both scaling curves are similar nevertheless and could indeed be brought to collapse by choosing a larger ξ for the longitudinal waves. That ξ depends somewhat on the type of mode is not surprising. However, it would be of course more appealing if one would have a simple physical argument explaining the *slower* crossover for longitudinal waves.

C. Eigenvectors: Noise and correlations

For periodic bulk systems of sufficiently large size, the low frequency modes turn out to be intricate linear superpositions of plane waves. But as the existence of the continuum limit for the largest of our systems is now sufficiently demonstrated we focus in the reminder of this paragraph on the *departure* from the continuum prediction.

In order to characterize the departure of the numerical eigenvector displacement fields $\underline{v}(p)$ from continuum theory we project them onto plane waves $\underline{v}_{\text{cont}}(q)$, i.e., we compute their Fourier amplitudes $A_p(q) = \langle \underline{v}(p) | \underline{v}_{\text{cont}}(q) \rangle$. This is shown in Fig. 11 for the eigenvectors $p = 3$, 11 and 27. The average $\langle \cdots \rangle$ is taken over the ensemble. The amplitudes are plotted versus $q - p$, i.e. we have shifted the abscissa axis horizontally in such a way as to emphasize the contribution of the pth elastic mode to the computed eigenvector with the same number. Indeed, the main contribution is seen to be due to the plane wave (propagative) mode with the same mode
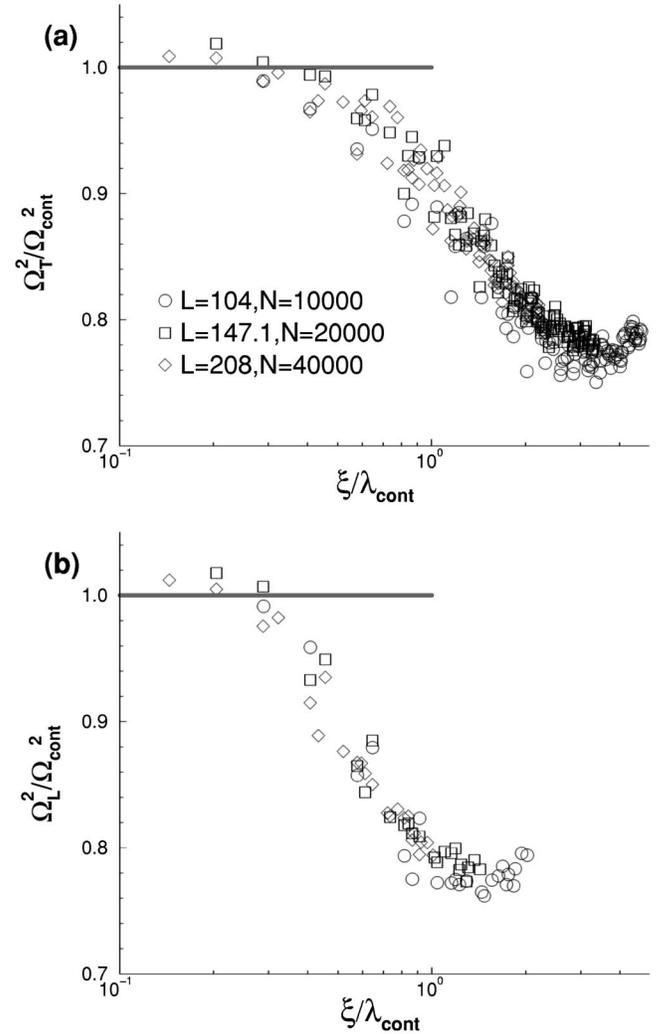
FIG. 10. Scaling of (a) transverse and (b) longitudinal modes for different box sizes as indicated. The rescaled frequency $\Omega^2/\Omega^2_{\text{cont}} = \langle \omega^2 \rangle / \omega^2_{\text{cont}}$ is plotted versus the inverse wavelength $\xi/\lambda_{\text{cont}}$. The theoretically expected wavelength $\lambda_{\text{cont}} = L/(n^2+m^2)^{1/2}$ is given by the quantum numbers (n,m) associated with the mode index p. We have again set $\xi \equiv 30a$. The crossover to continuum theory occurs at $\lambda \approx \xi$ for transverse modes and at about twice as large wavelengths for longitudinal modes. The success of both scaling plot suggests that ξ is frequency independent for sufficiently large system sizes where $\lambda(p) \ll L$, but does depend the wave type. We regard this as the new central results of this paper.

number. The three particular eigenvectors considered in Fig. 11, belong to sets of fourfold degenerate eigenstates. Hence, if noise could be discarded the projections onto plane waves would be of width four, corresponding to an average over all possible random phases. Accordingly, the projection of eigenvectors belonging to an eightfold degenerated set would have a width eight (not shown). As anticipated by our discussion of the eigenvalues the overlap between numerical and theoretical eigenmodes deteriorates with increasing mode index p. This is seen from the decreasing peak height and the increasing width of the function $A_p(q-p)$ with increasing p. The enlargement of the peak to neighboring fre-
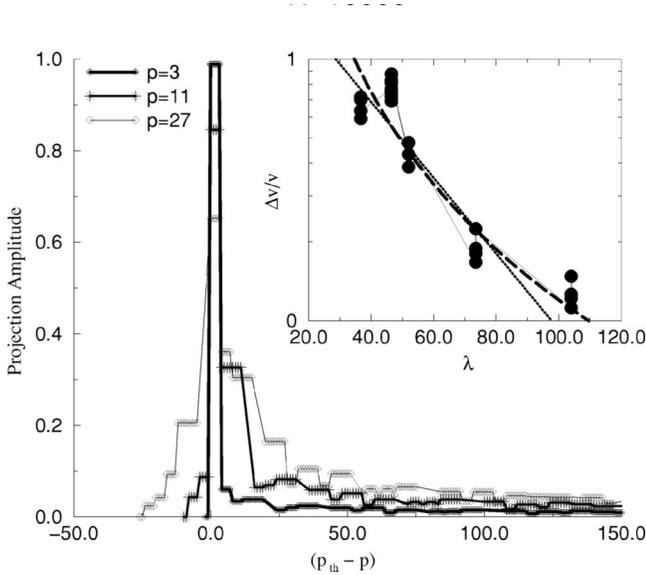
FIG. 11. Construction of noisy eigenvector field for periodic box configurations with $N = 10\,000$, $\rho = 0.925$. Main figure: projection amplitude of empirical eigenvectors $p = 3$, 11, and 27 on the theoretical plane waves which are indexed with q with increasing frequency. Only the transverse modes are included for clarity. Insert: relative amplitude of noise as a function of wavelength $\lambda(p)$. The dotted line is a fit with $\exp(-\lambda_{\text{cont}}/30a)$ in agreement with the estimation $\xi \approx 30a$ for the characteristic wavelength. The long-dashed line is a fit with λ^{-2} in agreement with a scattering process.

quencies suggests a scattering process in agreement with Refs. 16,17. Note the asymmetric character of the projections amplitudes, which must vanish for $q < 3$. Interesting, even for small p, the amplitudes do not completely vanish for large $q - p$, but become more or less constant. This indicates a Fourier transformed *localized* noise term, in agreement with the quasilocalized modes described in Ref. 14. As we shall elaborate now below, this is due to vortices in analogy to those depicted in Fig. 5.

The next step consists in the construction of the noise field by substracting the contributions of the dominant peak from the numerical eigenvectors $\underline{v}(p)$,

$$\delta\underline{v}(p) \equiv \underline{v}(p) - \sum_{q \in \mathcal{D}_p} A_p(q)\underline{v}_{\text{cont}}(q), \qquad (11)$$

where $\mathcal{D}_p$ is the set of 4 (or 8) plane waves q that contribute most to the Fourier decomposition of the mode p. Obviously, $\|\delta\underline{v}(p)\| = \sqrt{\Sigma_{q \notin \mathcal{D}_p} A_p(q)^2}$ should decrease with the wavelength. We have computed the dimensionless ratio $\|\delta\underline{v}(p)\|/\|\underline{v}(p)\|$ and plotted this quantity in the inset of Fig. 11 vs the wavelength $\lambda_{\text{cont}}(p)$. This curve is in qualitative agreement with a scattering process of Rayleigh type,[17] where $\|\delta\underline{v}(p)\|/\|\underline{v}(p)\| \propto \lambda^{-2}$. We have compared the data with the exponential decay $\exp(-\lambda_{\text{cont}}/30a)$. Interestingly, the characteristic wavelength defined here is equal to ξ. Our data do not allow us to discriminate between both fits. The conclusion is thus that, whatever the origin of the noise (scattering process or not), the noise is small compared to the propagative theoretical mode when $\lambda \gg \xi$.
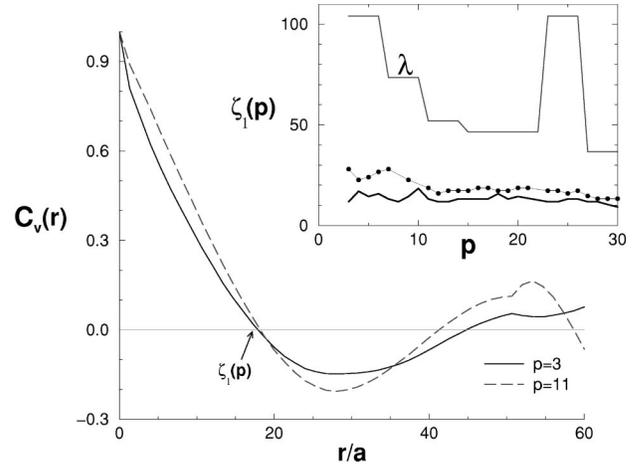
FIG. 12. Correlation function $\langle \delta\underline{v}_p(r)|\delta\underline{v}_p(0)\rangle$ of the eigenvector noise fields for $p = 3$ and 11 vs distance r. The curves are similar to the ones shown in Fig. 6(a) and feature again prominent anticorrelations. Inset: $\zeta_1(p)$ characterizing the anticorrelation for $N = 10\,000$ (dotted line) and $N = 5\,000$ (bold line). Also included is the wavelength from Eq. (3) associated with each continuum mode (top line).

Let us now study the structure of the noisy part of the wave vector. Assuming a scattering process, it would be particularly interesting to determine the dependency of a possible mean free path into the wavelength λ_{cont} of the eigenmode. Two examples for eigenvector noise fields $\delta\underline{v}(p)$ are presented in Figs. 5(c) and 5(d) for the modes $p = \overline{3}$ and $p = 7$, respectively. They are compared with the non-affine fields obtained for the same configuration in an elongational and pure shear displacement field. The vortices are again the most striking features. The four fields given look indeed remarkably similar: The sizes and positions of the vortices are obviously highly correlated. To put this in quantitative terms we consider correlation functions for the eigenvector noise fields designed in analogy to those discussed for the nonaffine fields.

The correlation function $C_v(r) \equiv \langle \delta\underline{v}(r)|\delta\underline{v}(0)\rangle$ is presented in Fig. 12 for two modes $p = \overline{3}$ and $p = 11$. As expected from the noise field snapshots we find again the anticorrelations similar to those presented for the nonaffine fields in Fig. 6(a). The anticorrelation extends even to somewhat larger distances. We realize that the mode dependence while visible is weak. In the inset we have plotted the first node of the anticorrelation $\zeta_1(p)$. Also included is the wavelength corresponding to the mode number p. We find that ζ_1 does not vary much with λ, unlike the λ^4-dependence of the mean free path in scattering processes. Thus the noise displays a characteristic length ζ_1 comparable to ξ and independent on the mode p. We stress that the resulting participation ratio of the noise is weak, thus our results are in complete agrement with previous works on (quasi-)*localized* modes.[14] However, the slow (non exponential) decay of the correlation function is also in favor of *delocalization*.[15,20]

VII. DISCUSSION

In summary, we have presented extensive simulations of mechanical and low-frequency vibrational properties of

quenched amorphous disk-shaped aggregates and periodic bulk systems. Two-dimensional ensembles containing up to 40 000 polydisperse Lennard-Jones particles have been generated and analyzed in terms of sample size, density, sample symmetry, and quench protocol. We have focused on systems with densities close to the zero-pressure state to have similar conditions for the two boundary symmetries studied. The eigenmodes of the structures are calculated by diagonalization of the dynamical matrix and the eigenfrequencies are compared with the predictions from classical continuum theory where we concentrate on the low frequency end. The second key calculation we performed consists in macroscopic deformations (pure elongation and pure shear) of a periodic box in order to obtain the elastic moduli (Lamé coefficients) and the microscopic displacement fields. These are in turn compared with the noisy part of the corresponding eigenvector fields.

The central results of this study are as follows:

(1) The application of continuum elasticity theory is subject to strong limitations in amorphous solids, for system sizes below a length scale ξ of typically 30 interatomic distances. This length scale is revealed in a systematic finite-size study of the eigenfrequencies and in the crossover scaling of modes p for fixed system size with the wavelength $\lambda(p)$. This size is much larger than the discretization, and sound wave dispersion is of course irrelevant at this scale.

(2) The success of the scaling of the eigenfrequencies with the wavelength demonstrates that ξ is a *critical wavelength*. It is within numerical accuracy independent of the mode and of the system size. The crossover behaviors of transverse and longitudinal modes are similar, although the latter is somewhat slower, i.e., slightly larger systems are required to match the same mode with continuum theory.

(3) The macroscopic deformation experiments demonstrate that the nonaffine displacements of the atoms on the local scale matter: a finite amount of energy is stored in the nonaffine field and there is a large difference between the true Lamé coefficients and those obtained from the dynamical matrix, assuming an affine displacement field on all scales.

(4) Below a length scale similar to ξ both the nonaffine displacement field and the noisy part of the eigenvector fields displays vortex-like structures. These structures are responsible for the striking anticorrelations in the vectorial pair correlation functions of both types of fields. We have identified in this paper the nonaffine field as the central microscopic feature that makes the continuum approach inappropriate.

Inhomogeneities in local elastic coefficients, are an essential ingredient in several recent calculations on disordered elastic systems.[11,12] Indeed, the origin of the departure from elastic behavior seen in the two key computer experiments is ultimately related to the local disorder. This disorder is revealed by the structure of the force network frozen into the solid, as shown in Fig. 1. Interestingly, weak finite-size effects are evidenced in properties of the frozen local disorder like the pressure, the particle energy and one of the Lamé coefficients and in the histograms of forces, coupling constants and dynamical matrix trace.

Surprisingly at first sight, we have been unable to identify a sufficiently large length scale solely from the frozen local disorder. There must be a mechanism which amplifies these in such a way that the deformation fields as the ones displayed in Fig. 5 become nonaffine on scales comparable to $\xi = 30a$. Incidentally, this mechanism is not directly related to the mean free path that can be computed in diffusion processes[17] as can be shown by the absence of any λ-dependence. The Rayleigh scattering thus appears not to be the unique way to localization. One marked difference is that the mean free path is obtained in one-dimensional models,[17,18] however the characteristic length is related in our study to vortices, implying a displacement in the transverse direction. A one-dimensional model of the displacement field in a two-dimensional medium as in Ref. 18 appears thus to be unrealistic. Unfortunately, we are not able at the moment to propose a definite relation between the size of the vortices and the local properties of the system. Preliminary studies[39] suggest a strong correlation between the vortices and the occurrence under mechanical solicitation of nodes of stresses acting as bolts and forcing a displacement in the transverse direction. This must be related to the local anisotropy of forces as already been suggested in Ref. 40 in another context.

Interestingly, sizes similar to ξ, or somewhat smaller, are often invoked,[9,10] as typical of the heterogeneities that give rise to anomalies in the vibrational properties of disordered solids (glasses) in the Terahertz frequency domain, the so-called boson peak. In particular, Ref. 9 considers the existence of rigid domains separated by softer interfacial zones, not unlike those revealed by the nonaffine displacement pattern of Fig. 5(a). Our work offers a new vantage point on this feature. Inhomogeneities of size ξ (corresponding to Thz frequency) in the displacement field could provide an interpretation of the discrepancy between the measured vibrational density of states and that of a continuum, elastic model (the Debye model).

The present study documents the importance of systematic finite-size characterizations for the computational investigations of glassy systems well below the glass transition. It suggests that numerical investigation of vibrational properties should systematically make use of samples much larger than ξ, in order to avoid finite-size effects and to be statistically significant. Too small systems tend to be slightly more rigid and have higher pressures and system energies.

Finally, let us mention that such vortices have been studied in disordered materials in the context of large deformations and flow.[20,24] We show here that the same mechanism happens even in the elastic regime, for very small deformations in a quasistatic motion. Vortex-like deformation patterns have also been identified, and associated with, in simulations of granular materials.[41] Our studies clearly shows that very simple models, involving only conservative forces, are sufficient to reproduce such patterns. Disorder appears to be much more relevant than the "granular" aspect (e.g., frictional terms) for this type of property.

The above conclusions are obviously subject to the conditions under which our simulations have been performed. The most serious limitation of this work is certainly that we have only reported results on two-dimensional samples. Of

course, one expects correlations to be reduced in higher dimensions and finite-size effects should be less troublesome there. However, this study initially originated from an attempt to compute the vibrational modes of three dimensional clusters. Surprisingly, we have been unable to reach there the elastic limit even for systems containing 10 000 atoms and had to switch to the simpler two dimensional case which is in terms of particle numbers less demanding even though the length scale ξ might ultimately turn out to be smaller in three dimensions. Indeed, we believe that a systematic finite-size analysis of mechanical and vibrational properties in three-dimensional amorphous bodies is highly warranted and we are currently pursuing simulations in this direction.

Other system parameters like the polydispersity index and specifically the quench protocol should be systematically altered to further the understanding of the origins of the demonstrated correlations. We have not seen within the accuracy of our data any systematic effect of the quench protocol on the the characteristic length ξ. However, more attention should certainly be paid to the aging processes occurring in quenched samples as a function of system size.

*Email address: atanguy@dpm.univ-lyon1.fr

[1] A.C. Eringen and E.S. Suhubi, *Elastodynamics* (Academic, New York, 1975).

[2] L.D Landau and E.M. Lifshitz, *Theory of Elasticity* (Butterworth-Heinemann, London, 1995).

[3] P.M. Chaikin and T. C. Lubensky, *Principles of Condensed Matter* (Cambridge University Press, Cambridge, 1995).

[4] S. Alexander, Phys. Rep. **296**, 65 (1998).

[5] N.D. Fatti, C. Voisin, F. Chevy, F. Vallée, and C. Flytzanis, J. Chem. Phys. **110**, 11 484 (1999).

[6] M. Nisoli, S. De Silvestri, A. Cavalleri, A.M. Malvezzi, A. Stella, G. Lanzani, P. Cheyssac, and R. Kofman, Phys. Rev. B **55**, R13 424 (1997).

[7] J.H. Hodak, I. Martini, and G.V. Hartland, J. Phys. Chem. **108**, 9210 (1998); J. H. Hodak, A. Henglein, and J. V. Hartland, *ibid.* **112**, 5942 (2000).

[8] L. Saviot, B. Champagnon, E. Duval, and A.I. Ekimov, Phys. Rev. B **57**, 341 (1998); B. Palpant, H. Portales, L. Saviot, J. Lermé, B. Prével, M. Pellarin, E. Duval, A. Perez, and M. Broyer, *ibid.* **60**, 17 107 (1999); H. Portales, L. Saviot, E. Duval, M. Fujii, S. Hayashi, N. Del Fatti, and F. Vallée, J. Chem. Phys. **115**, 3444 (2001).

[9] E. Duval, L. Saviot, A. Mermet, L. David, S. Etienne, V. Bershtein, and A.J. Dianoux (unpublished); G. Viliani, E. Duval, and L. Angelani (unpublished); E. Duval and I. Mermet, Phys. Rev. B **58**, 8159 (1998).

[10] A.J. Dianoux, W. Petry, and D. Richter, *Dynamics of Disordered Materials* (North–Holland, Amsterdam, 1993).

[11] W. Schirmacher, G. Diezemann, and C. Ganter, Phys. Rev. Lett. **81**, 136 (1998).

[12] L. Angelani *et al.*, Phys. Rev. Lett. **84**, 4874 (2000).

[13] J.P. Wittmer, A. Tanguy, J.-L. Barrat, and L. Lewis, Europhys. Lett. **57**, 423 (2002).

[14] V.A. Luchnikov, N.M. Medvedev, Yu.I. Naberukhin, and H.R. Schober, Phys. Rev. B **62**, 3181 (2000); H.R. Schober and C. Oligschleger, *ibid.* **53**, 11 469 (1996); H.R. Schober and B.B. Laird, *ibid.* **44**, 6746 (1991).

[15] V. Mazzacurati, G. Ruocco, and M. Sampoli, Europhys. Lett. **34**, 681 (1996).

[16] S.N. Taraskin and S.R. Elliott, in *Physics of Glasses*, edited by Jund and Jullien, AIP Conf. Proc. No. 489 (AIP, New York, 1999).

[17] P. Sheng, *Introduction to Wave Scattering, Localization, and Mesoscopic Phenomena* (Academic, San Diego, 1995).

[18] M. Leibig, Phys. Rev. E **49**, 1647 (1994).

[19] S. Melin, Phys. Rev. E **49**, 2353 (1994).

[20] F. Radjai and S. Roux, cond-mat/0205618 (unpublished).

[21] M.E. Cates, J.P. Wittmer, J.P. Bouchaud, and P. Claudin, Phys. Rev. Lett. **81**, 1841 (1998).

[22] M.E. Cates, J.P. Wittmer, J.P. Bouchaud, and P. Claudin, Chaos **9**, 511 (1999).

[23] A.J. Liu and S.R. Nagel, Nature (London) **396**, 21 (1998).

[24] S.A. Langer and A.J. Liu, J. Phys. Chem. B **101**, 8667 (1997).

[25] G. Debrégeas, H. Tabuteau, and J.-M. di Meglio, Phys. Rev. Lett. **87**, 178305 (2001).

[26] Ph. Claudin and E. Clément (unpublished).

[27] C. Kittel, *Introduction to Solid State Physics* (Wiley, New York, 1995).

[28] J. Salençon, *Handbook of Mechanics* (Springer-Verlag, Berlin, 2001).

[29] Note that both the wavelength and one of the Lamé coefficients are denoted by λ. To avoid ambiguity we write $\lambda(n,m)$, $\lambda(p)$ or λ_{cont} for the wavelength where necessary.

[30] Note that in 2D, the upper bound for the Poisson ratio is 1 and not 1/2 as in 3D.

[31] D.R. Squire, A.C. Holt, and W.G. Hoover, Physica (Amsterdam) **42**, 388 (1969).

[32] It is instructive to consider the simple one-dimensional analogy, i.e., a long string of connected springs with force constants c_l, to appreciate the approximation made in the above equations. We recall that the effective macroscopic Young modulus is $\lambda = 1/\langle 1/c_l \rangle$ rather than $\lambda_a = \langle c_l \rangle$. This is due to the fact that the tension along the chain is constant but *not* the displacement field. Hence, Eqs. (9) are in general only good approximations if the dispersion of the effective spring constants is small and an external macroscopic strain is locally transmitted in an affine way. (λ is then indeed given by the mean coupling constant with a *negative* quadratic dispersion correction in leading order.)

[33] I. Goldhirsch and C. Goldenberg, cond-mat/0203360 (unpublished).

[34] M.P. Allen and D.J. Tildesley, *Computer Simulations of Liquids* (Oxford Science, Oxford, 1987).

[35] J.M. Thijssen, *Computational Physics* (Cambridge University Press, Cambridge, 1999).

[36] W. H. Press *et al.*, *Numerical Recipes* (Cambridge University Press, 1982).

[37] S. Pinker, *How the Mind Works* (Penguin, New York, 1999).

[38] J.Y. Choi, J.J. Dongarra, R. Pozo, D.C. Sorensen, and D.W. Walker, Int. J. Supercomput. Appl. **8**, 99 (1994).

[39] A. Tanguy and J. Wittmer (unpublished).

[40] A. Tanguy and P. Nozières, J. Phys. I **6**, 1251 (1996).

[41] J.R. Williams and N. Rege, Powder Technol. **90**, 187 (1997); M.R. Kuhn, Mech. Mater. **31**, 407 (1999); J-N. Roux and G. Combe, C.R. Phys. **3**, 131 (2002).